Received: 29 November 2023 | Revised: 5 February 2024 | Accepted: 16 February 2024

DOI: 10.1002/ces2.10211

International Journal of Ceramic Engineering & Science

RESEARCH ARTICLE

X-ray computed tomography study of microstructure weakening by high-temperature hydrogen attack on refractories

Anita Razavi | **Isabelle Henn** | **Almuth Sax** | **Peter Quirmbach**

Institute for Natural Sciences, Technical Chemistry and Corrosion Sciences, University of Koblenz, Koblenz, Germany

Correspondence
Anita Razavi, Institute for Natural Sciences, Department of Technical Chemistry and Corrosion Sciences, University of Koblenz, Universitaetsstr. 1, 56070 Koblenz, Germany.
Email: razavi@uni-koblenz.de

Funding information
European Union of the European Regional Development Fund and Rhineland-Palatinate, Grant/Award Number: 84004803; Consortium project "Refractories under Hydrogen Load" with the project partners Almatis GmbH, Refratechnik Steel GmbH, Steuler KCH GmbH and ThyssenKrupp Steel Europe AG; Open Access Fund of the University of Koblenz

Abstract

X-ray computed tomography (XRT) is a three-dimensional (3D), non-destructive, and reproducible investigation method capable of visualizing and examining internal and external structures of components independent of the material and geometry. In this work, XRT with its unique abilities complements conventionally utilized examination methods for the investigation of microstructure weakening induced by hydrogen corrosion and furthermore provides a new approach to corrosion research. The motivation for this is the current inevitable transformation to hydrogen-based steel production. Refractories of the system Al_2O_3-SiO_2 are significant as lining materials. Two exemplary material types A and B, which differ mainly in their Al_2O_3:SiO_2 ratio, are examined here using XRT. Identical samples of the two materials are measured, analyzed, and then compared before and after the hydrogen attack. In this context, hydrogen corrosion-induced porosity and its spatial distribution and morphology are investigated. The results show that sample B has a higher resistance to hydrogen-induced attack than sample A. Furthermore, the 3D representation revealed a differential porosity increase within the microstructure.

KEYWORDS
X-ray computed tomography, refractories, microstructure

1 | INTRODUCTION

Recently, X-ray computer tomography (XRT) has gradually established its position as a non-destructive and thus reproducible three-dimensional (3D) investigation technique allowing material and geometry-independent application. The technique uses X-rays to generate multiple two-dimensional (2D) projections from distinct angles, which are subsequently reconstructed into a 3D image.[1]

As the object rotates within the X-ray beam between the X-ray source and the detector, a defined number of 2D projections from different angles are scanned. Each projection corresponds to the object profile at one angle and is obtained from the attenuated X-rays. The attenuation can be described using the following equation[2]:

$$I(L) = I_0(E)\, e^{-\int_0^L \mu(E,\, x)dx}\, dE \qquad (1)$$

I(L) describes the X-ray intensity after interaction with matter, $I_0(E)$ the X-ray intensity emitted by the source, and L the distance traveled by the X-rays in matter. For polychromatic X-rays and a heterogeneous medium, the formula includes the integral for varying attenuation coefficients μ along L and varying X-ray energies E.[2]

A 2D projection consists of a map of attenuation coefficients μ, describing the attenuation of X-rays by the object for each pixel within the scanned cross-section. The material-specific values of μ increase with density ϱ, atomic number Z, and path length L.[3] Specifically, μ increases with ϱ and Z^4.[1]

In an XRT scan, varying attenuation values are visualized in different shades of gray. While highly absorbent materials are represented in bright shades, less absorbent areas are represented in darker shades of gray.[4]

In a previous study, XRT was used to examine bauxite leached with hydrochloric acid.[5] The focus was to measure the penetration depth of acid, porosity, and its distribution in individual bauxite grains. In this work, XRT will be adapted to evaluate the microstructure weakening of Al_2O_3-SiO_2 refractories attacked by hydrogen.

To reduce greenhouse gas emissions, especially CO_2, the steel industry is currently shifting towards hydrogen-based steel production. The Climate Protection Act (§3[2]) of the Federal Government of Germany, containing the goal of greenhouse gas neutrality by the year 2045, motivates this change. In 2018, the steel industry generated approximately 30% of the CO_2 emissions of the entire German industry.[6] Thus, the transformation of steel production is inevitable. Process-related emissions are mainly generated using carbon-containing reducing agents in blast furnaces.[7] To achieve climate-neutral steel production in the future, the use of hydrogen as a reducing agent in pig iron production promises high potential, for example, in direct reduction plants.[8,9] Refractory linings of steelmaking plants are also exposed to the reducing gas. To ensure long-term use of these oxide refractories, high-temperature hydrogen environment stability is essential. Thus, the demands on refractories of the lining are extended, especially regarding hydrogen resistance.

Among others, refractories of the system Al_2O_3-SiO_2 are considered for use in pig iron production.[10] Based on their application and technical requirements, these refractories differ in their Al_2O_3:SiO_2 ratio. In this study, two exemplary materials of the system Al_2O_3-SiO_2 based on mullite-fireclay and corundum-mullite are investigated. According to previous studies, SiO_2 is critical with respect to hydrogen attack under high-temperature conditions.[11–13] Consequently, hydrogen attack on SiO_2 leads to weight loss due to the formation of the gaseous products SiO and H_2O. This is described by the following equation[11]:

$$SiO_2\,(s) + H_2\,(g) \rightarrow SiO\,(g) + H_2O\,(g) \qquad (2)$$

Accordingly, increasing weight loss indicates higher corrosion and thus increasing hydrogen attack.[11–14] This is reflected in the sample microstructure, including increased pore volume.

The common approach for the investigation of hydrogen corrosion consists of several different analytical methods. These include weight loss determination, cold compressive strength (CCS) measurements, scanning electron microscopy (SEM), and X-ray diffraction (XRD).[11,12,15–17]

Weight loss is the first indication that hydrogen attack has weakened the microstructure. CCS determines the mechanical strength of the material before and after the hydrogen attack. SEM is used to locally examine the microstructure optically at selected cross-sections in high resolution, providing insight into this restricted area. Although limited to two dimensions, combined with energy-dispersive X-ray spectroscopy (EDX) microanalysis, it allows the chemical characterization of a cross-section. XRD is applied to identify changes in the mineral phases due to hydrogen-induced attack. However, CCS, SEM, and XRD destroy the sample during the examination, thereby eliminating the possibility of comparative measurements of the same sample before and after the hydrogen attack.

In this work, XRT is used to further investigate the microstructure before and after hydrogen attack. It allows a spatial characterization of porosity induced by corrosion. Additionally, potential gradients in the pore distribution can be identified. For a comprehensive evaluation of hydrogen corrosion, XRT is utilized as a complementary method to the conventionally used analysis methods. Weight loss determination and SEM are considered in the following, as they provide comparative information regarding the microstructure.

However, to our knowledge, XRT has not been used to investigate the influence of hydrogen-induced attack on the microstructure of refractories. It provides a holistic volumetric insight into the samples and, due to its non-destructive property, enables a comparison before and after the attack. Furthermore, XRT allows the determination of the distribution and morphology of porosity.

Here, XRT is applied for the comparative evaluation of two exemplary refractories of the system Al_2O_3-SiO_2 regarding their hydrogen resistance. As an optically based method, XRT extends the limited insight into the microstructure of the samples provided by SEM studies and offers a different perspective on hydrogen corrosion.

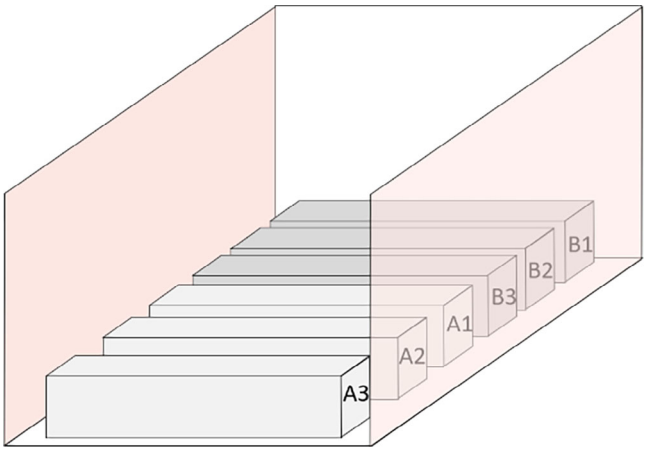

FIGURE 1 Schematic furnace installation. The heating elements are located left and right of the samples on the red highlighted walls.

2 | MATERIALS AND METHODS

2.1 | X-ray fluorescence of reference samples

In this work, three sample bars each of two exemplary Al_2O_3-SiO_2 refractories (A and B) were investigated. X-ray fluorescence (XRF) was used to characterize the chemical properties of the untreated samples. The analyses were quantitatively carried out using lithium tetraborate melt tablets according to DIN EN ISO 12677[18] using a Bruker S8 TIGER wavelength dispersive XRF spectrometer.

2.2 | Hydrogen attack

Hydrogen corrosion tests of Al_2O_3-SiO_2 refractories A and B were performed in each case on three bars with dimensions of 150 mm x 25 mm x 25 mm in a Linn High Therm HT-1600-GT-Sonder chamber furnace (Figure 1). An exposure time of t = 200 h at a temperature of T = 1400°C under atmosphere pressure in a 100% hydrogen atmosphere (purity 5.0) was selected for the tests.

2.3 | Scanning electron microscopy

SEM investigations were performed with a Zeiss EVO 15 and coupled EDX using an Oxford Instruments Ultimax 65 EDX detector. The examinations were carried out on prepared, that is, sawn, subsequently embedded, polished, and carbon-sputtered micro-sections of one exemplary sample for each material after the hydrogen attack. The images were generated using backscattered electrons at an accelerating voltage of U = 15 kV. In addition, coupled EDX mappings of the elements Al and Si were acquired.

TABLE 1 Chemical compositions of materials A and B.

Component	Mass fraction material A (wt%)	Mass fraction material B (wt%)
Al_2O_3	61.89	89.90
SiO_2	34.52	9.52
Fe_2O_3	1.07	0.12
TiO_2	1.69	0.07
Impurities (CaO, MgO, alkalies, etc.)	0.83	0.39

2.4 | X-ray computed tomography examination

The examination of the Al_2O_3-SiO_2 refractories A and B before and after the hydrogen attack was performed using a ProCon X-Ray CT-Alpha Duo system. The samples were evaluated with the microfocus tube at U = 235 kV and a radiation power of P = 59.9 W. The polychromatic beam was filtered using a 1 mm copper filter. The flat panel detector provides a matrix of 2048 × 2048 pixels with a pixel pitch of 200 µm. The sample size with the corresponding focus-detector-distance and the focus-object-distance results in a voxel size of 88.44 µm.

The evaluation and visualization of the XRT data was carried out with the software VGStudio Max from Volume Graphics GmbH. The surface determination of the investigated sample was performed by VGStudio's advanced (classic) option, based on the starting contour from the histogram with automatic material definition at an ISO value of 50%. Based on the results of the surface determination, the porosity/inclusion analysis module (VGDefX/Only threshold algorithm) of the VG Studio software was selected for the identification of voids in the samples before and after the hydrogen attack. The threshold used for pore segmentation is obtained from a manually selected representative region of the background and material.

3 | RESULTS AND DISCUSSION

3.1 | XRF results of reference samples

The XRF results of the two materials A and B are shown in Table 1. Here, the chemical composition is displayed in wt%. It is evident that the chemical composition of the two materials mainly differ in their Al_2O_3:SiO_2 ratio. While material A has an Al_2O_3 content of 61.89 wt% and SiO_2

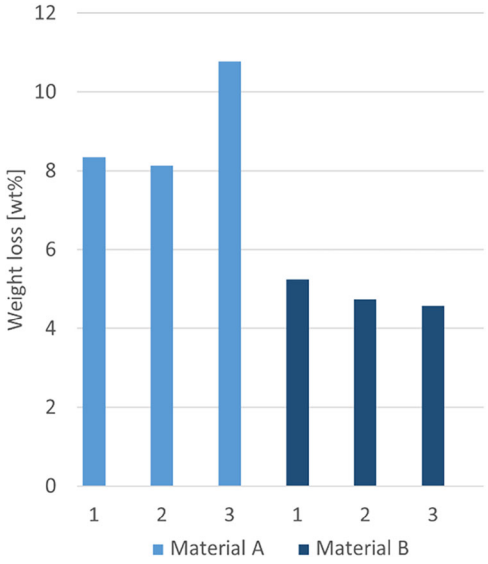

FIGURE 2 Results of the weight loss determination. The X-axis shows the samples 1–3 for the respective materials A and B.

content of 34.52 wt%, material B has a higher Al_2O_3 content of 89.90 wt% and correspondingly a lower SiO_2 content of 9.52 wt%. In addition, material A has a higher iron oxide and titanium oxide content compared to material B.

3.2 | Weight loss results

The results of the weight loss determination are presented in Figure 2. Material A reveals a higher weight loss compared to material B. This provides the first indication of a more severe hydrogen attack on material A, which is attributed to the higher SiO_2 content.

3.3 | SEM results

In Figure 3A, the BSE-SEM image of the corrosion zone of the exemplary sample A2 reveals a clear damage pattern after the hydrogen attack. Damage is evident from loss of substance and highly porous areas which represent the corrosion zone. Figure 3B shows the result of an Al and Si mapping. Al is represented in blue and Si in red. The Si depletion in the porous areas respectively in the corrosion zone is obvious.

Figure 4A accordingly shows the BSE-SEM image of the corrosion zone of B2 after hydrogen attack. A damage pattern due to loss of substance and porous areas is also evident here. Note that only sections of the corrosion zone of both materials were selected and examined. The comparison of these sections indicates a less pronounced corrosion zone in B2 than in A2. This is reflected in the significantly lower porosity. Figure 4B nevertheless shows a clear Si depletion in the corrosion zone of B2.

3.4 | X-ray computed tomography results

The focus of the investigations is the spatially resolved determination of the influence of hydrogen attack on the microstructure, particularly on the pore volume of the two Al_2O_3-SiO_2 refractories. Due to the non-destructive nature of XRT, identical samples are scanned, analyzed, and visualized before and after the hydrogen attack. The reconstructed volume of the untreated sample is digitally compared with the volume of the subsequently corroded sample to identify the influence of hydrogen attack on the microstructure respectively the pore distribution. However, to investigate complete samples, it is necessary to compromise on spatial resolution. Thus, pore diameters smaller than the voxel size (88.44 µm) are not properly characterized and are therefore not considered, resulting in no quantification of the total pore volume. Furthermore, note that all measurements provide a snapshot of the hydrogen corrosion influence on the microstructure after $t = 200$ h.

The XRT images provide insight into the internal microstructure and pore distribution. Figure 5 illustrates the corrosion zones in 2D-XRT images by comparing the untreated (top) and corroded (bottom) sample A2 through the darker areas on the sample surface. The corrosion zone depth is approximately 4–5 mm. Direct comparison shows the spatially strongest corrosion at the surface, especially at the sample ends, next to the heating elements in the furnace (Figure 1). The porosity analysis clearly illustrates this observation.

Figure 6 shows the porosity analysis results in 2D according to the color bar, revealing the pore distribution. The 2D-XRT image represents an example cross-section from the 3D data set. The following observations are representative of all cross-sections within the sample. Due to the hydrogen attack, the pore volume, which was homogeneously distributed in the sample before (top), increases strongly at the surface. Referring to the schematic furnace installation of the samples (Figure 1), it is obvious that the porosity increases at the top and especially at the sample ends. The bottom of A2 has a correspondingly smaller increase in porosity.

Note that the pore distribution within the microstructure varies for all three samples of material A after hydrogen-induced attack. Like A2, the porosity in A1 occurs more at the ends and top of the samples. However, A1 shows a stronger increase in porosity at the bottom after hydrogen attack than A2. A3, like the other two samples, has the highest porosity at its ends, but has a

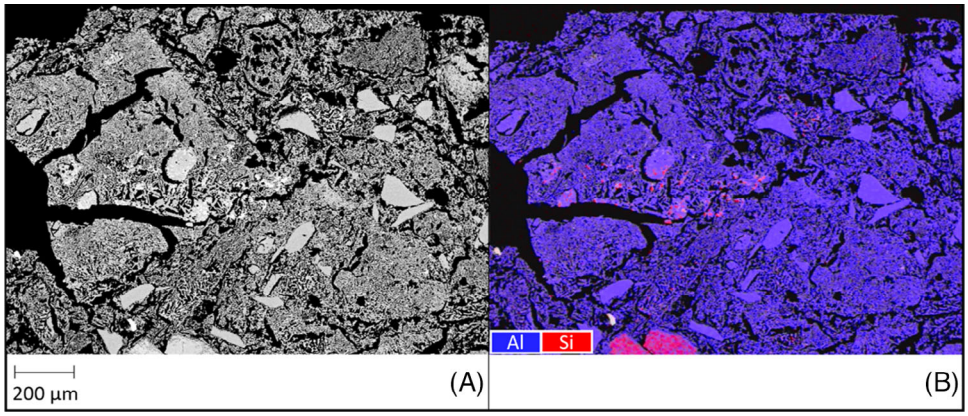

FIGURE 3 (A) Backscattered electron-scanning electron microscopy (BSE-SEM) scan of the corrosion zone of the exemplary sample A2 after hydrogen attack and (B) additional energy-dispersive X-ray spectroscopy (EDX) analysis respectively Al- and Si-mapping.

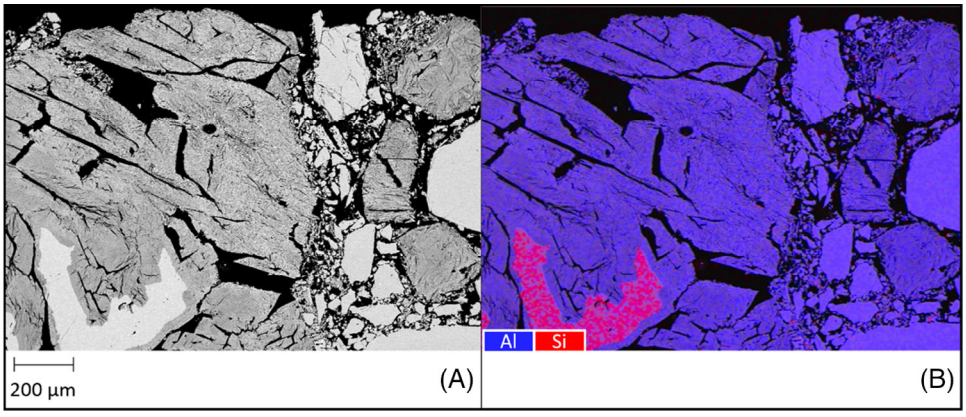

FIGURE 4 (A) Backscattered electron-scanning electron microscopy (BSE-SEM) scan of the corrosion zone of the exemplary sample B2 after hydrogen attack and (B) additional energy-dispersive X-ray spectroscopy (EDX) analysis respectively Al- and Si-mapping.

higher porosity at the bottom. This reveals a differential porosity increase in the microstructure of all samples and thus an uneven hydrogen attack. The increased porosity at the sample ends could be due to their position respectively proximity to the heating elements. Two explanations could be considered. The first one would be a temperature gradient within the furnace. However, this can be neglected due to the limited furnace volume of V = 32.5 L.

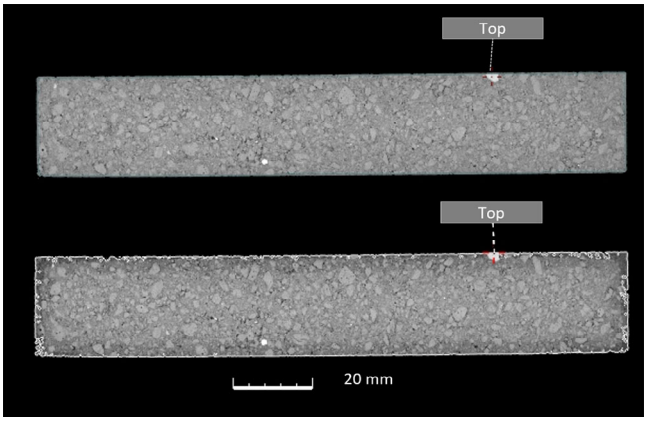

FIGURE 5 Two-dimensional-X-ray computed tomography (2D-XRT) image of A2 before (top) and after (bottom) hydrogen attack.

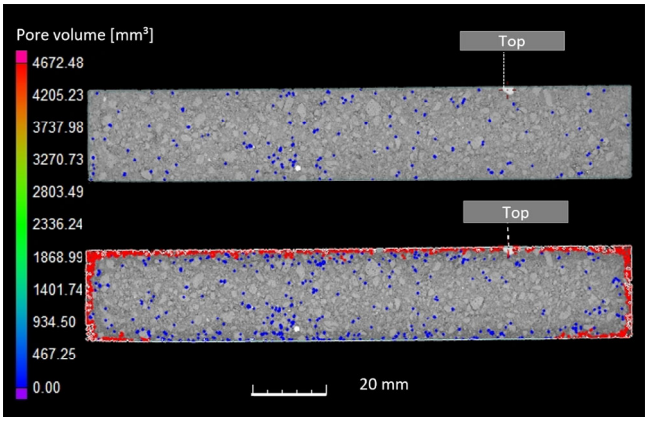

FIGURE 6 Two-dimensional (2D)-color representation of the pore volume of A2 before (top) and after (bottom) hydrogen attack.

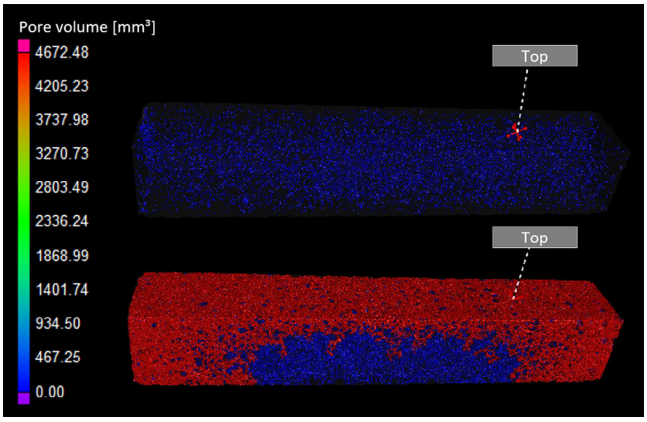

FIGURE 7 Three-dimensional (3D)-visualization of the pore volume of A2 before (top) and after (bottom) hydrogen attack. The sample itself is transparent, revealing the pore volume, visualized by the color bar.

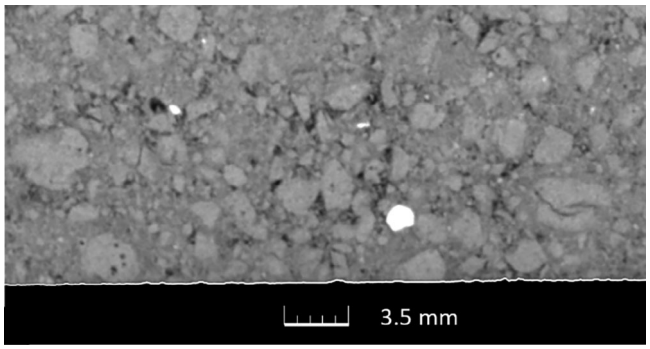

FIGURE 8 Magnification of two-dimensional-X-ray computed tomography (2D-XRT) image of A2 before hydrogen attack.

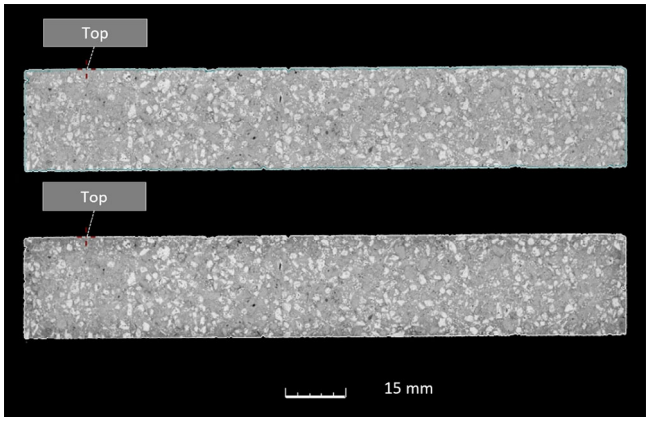

FIGURE 9 Two-dimensional-X-ray computed tomography (2D-XRT) image of B2 before (top) and after (bottom) hydrogen attack.

Another plausible explanation would be a flow gradient of the hydrogen gas within the furnace. This would be most pronounced at the heating elements and decrease towards the furnace's center. Without further investigations, no conclusive explanation can be given for the spatially inhomogeneous pore distribution at the top and bottom of the samples. This could be due to the position of the sample in the furnace or the sample itself.

Figure 7 illustrates the 3D-pore volume respectively the pore distribution of sample A2 before (top) and after (bottom) hydrogen attack. The sample itself is displayed transparently, revealing the 3D-color-coded pore volume. Before the hydrogen attack (top), a spatially homogeneous distributed porosity of smaller pores highlighted in blue is visible. The 3D representation of the pore volume after the hydrogen attack (bottom) illustrates the uneven pore distribution. The red-colored pores show enlarged and connected pores in the corrosion zone at the top and especially at the sample ends.

Additionally, XRT allows the localization of impurities. Table 1 displays an increased iron oxide (1.07 wt%) and titanium oxide (1.69 wt%) content in material A compared to material B. Due to the high atomic number ($Z_{Fe} = 26$, $Z_{Ti} = 22$), they are illustrated by white pixels in contrast to the main components Al_2O_3 ($Z_{Al} = 13$) and SiO_2 ($Z_{Si} = 14$), which are represented in varying shades of gray. This is exemplified in Figure 8 by a magnification of the 2D-XRT image of A2.

The 2D-XRT image of B2 before (top) and after (bottom) hydrogen attack in varying gray shades can be seen in Figure 9. A corrosion zone is evident in the corroded sample as well, recognizable by the darker gray shades represented on the sample surface. The 2D-grayscale images indicate that the corrosion zone of material B seems less developed than that of material A (Figure 5). The corrosion depth zone is approximately 3 mm.

The porosity analysis presented in Figure 10 confirms this observation. The figure shows an increased porosity at the sample surface after the hydrogen attack (bottom) in contrast to the untreated sample (top). Comparing this with the porosity analysis results of A2, a smaller corrosion zone and a lower pore volume in the corrosion zone are present. This is also observed for the other two samples of material B. In addition, a spatially different distributed porosity can be observed in all three samples.

The 3D representation of the results of the porosity investigation of B2 before (top) and after (bottom) hydrogen-induced attack in Figure 11 illustrates the lower porosity in the corroded state compared to material A. Furthermore, the pore size at the sample surface is smaller compared to Material A. This is reflected by the blue-colored pores at the sample surface. In addition, this pore volume representation reveals a homogeneous pore distribution within the corrosion zone. Isolated slightly larger pores, displayed in green are visible on the sample surface.

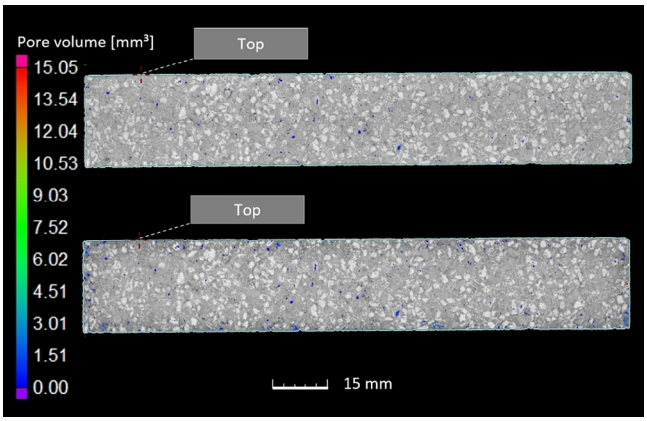

FIGURE 10 Two-dimensional (2D)-color representation of the pore volume of B2 before (top) and after (bottom) hydrogen attack.

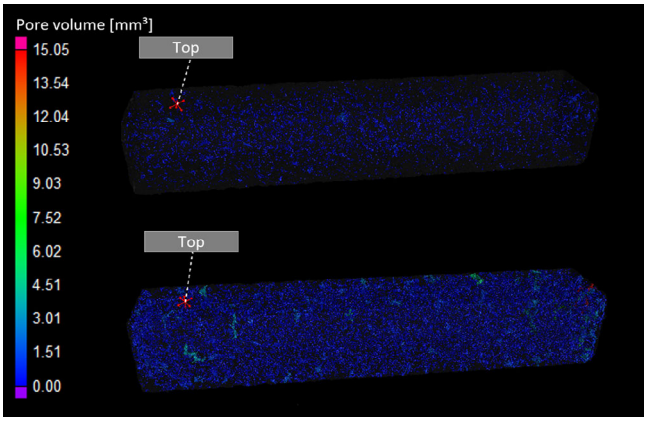

FIGURE 11 Three-dimensional (3D)-visualization of the pore volume of B2 before (top) and after (bottom) hydrogen attack. The sample itself is transparent, revealing the pore volume, visualized by the color bar.

Figure 12 provides an overview of the porosity analysis results of all samples, untreated (U) and after hydrogen attack (HA). The material volume is displayed in two blue tones depending on the material and the pore volume is in orange. The diagram confirms the above-presented results of the exemplary investigations of A2 and B2. It is evident that all samples of material A show increased porosity respectively corrosion after the hydrogen attack compared to all samples of material B.

4 | CONCLUSION

In this work, the influence of a hydrogen-induced attack under high-temperature conditions on the microstructure of two exemplary refractories of the system Al_2O_3-SiO_2 was evaluated.

For the investigation of hydrogen corrosion, conventional analysis methods exist, which, however, fail to provide information regarding the spatial distribution of the corrosion-induced porosity. Due to its non-destructive nature, XRT provides the unique possibility to spatially determine the porosity of identical samples before and after hydrogen attack.

The conventional analysis methods weight loss determination and SEM each show stronger hydrogen corrosion for material A compared to material B. This was already expected due to the higher SiO_2 content in material A. The XRT measurements confirm this and provide additional information about the spatial distribution and morphology of the pores before and after the hydrogen attack.

The porosity analysis for material A shows a homogeneous distribution of the untreated sample by the 3D-colored representation based on pore size. After a hydrogen-induced attack, an uneven pore distribution within the microstructure is revealed. Material B also has increased surface porosity after the hydrogen attack. The corrosion zone depth is less pronounced compared to material A, and the pore volume within the zone is also smaller. Thus, comparative studies reveal a higher resistance to hydrogen attack for material B than for material A.

The investigation after the hydrogen attack shows the strongest increase in porosity at the end of all samples, which are in proximity to the heating elements. This could indicate a flow gradient of the hydrogen gas within the furnace, resulting in different diffusion properties. Furthermore, the pore distribution varies for each of the three samples of the same material. Further investigations are necessary to determine the cause of the uneven pore distribution, for example, a correlation with the relative position of each sample in the furnace.

Further questions arise from the research and findings presented. In this work, the samples were analyzed and compared in an untreated state and after an exposure time of t = 200 h. To intensify corrosion research, the temporal and spatially resolved documentation of the pre-existing and corrosion-induced porosity, more precisely, the diffusion paths within the microstructure, is crucial. Thus, kinetic modeling of the corrosion depending on the corrosion zone depth is recommendable.

To fully consider progressive chemical corrosion reactions and processes, additional information on the product gas composition and mineralogical phase development is required. To investigate mass change and product gases, thermogravimetry coupled with a mass spectrometer could be used. SEM coupled with electron backscatter diffraction enables a localized analysis of mineralogical phase development.

XRT combined with various analysis methods, offers a comprehensive approach to gas corrosion in general. The

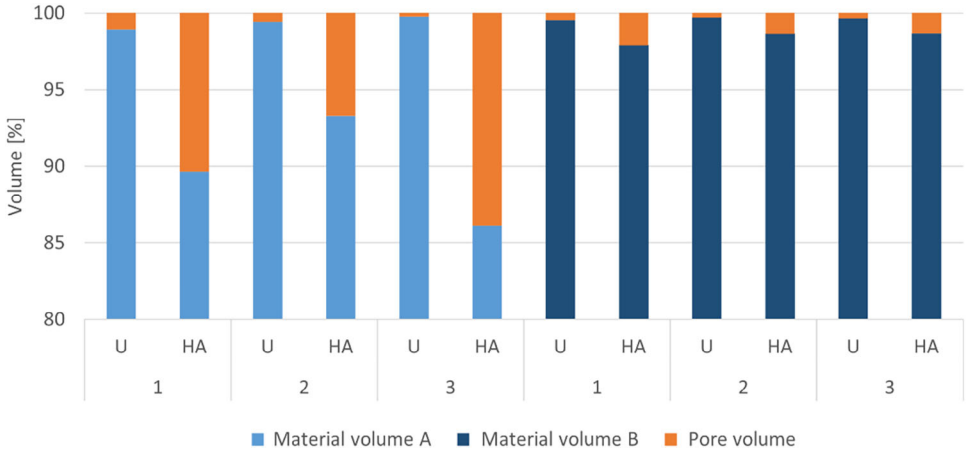

FIGURE 12 Overview of the porosity analysis results of samples A 1–3 and B 1–3, untreated (U) and after hydrogen attack (HA).

knowledge gained can aid in predicting corrosion processes and should be considered in material selection and development.

ACKNOWLEDGMENTS

This research was funded by the European Union of the European Regional Development Fund and Rhineland-Palatinate, project number: 84004803, consortium project "Refractories under Hydrogen Load" with the project partners Almatis GmbH, Refratechnik Steel GmbH, Steuler KCH GmbH and ThyssenKrupp Steel Europe AG and supported by the Open Access Fund of the University of Koblenz.

ORCID

Anita Razavi https://orcid.org/0009-0000-3105-1861

REFERENCES

1. Buzug TM. Einführung in die Computertomographie: Mathematisch-physikalische Grundlagen der Bildrekonstruktion. Berlin, Heidelberg: Springer; 2004.
2. Carmignato S, Dewulf W, Leach R. Industrial X-ray computed tomography. Cham: Springer International Publishing; 2018. Available From: https://Ebookcentral.Proquest.Com/Lib/Kxp/Detail.Action?Docid=5110718
3. Phillips DH, Lannutti JJ. Measuring physical density with X-ray computed tomography. NDT & E Int. 1997;30(6):339–50.
4. Romans LE. Computed tomography for technologists: A comprehensive text. Philadelphia, PA: Wolters Kluwer/Lippincott Williams & Wilkins; 2011. Available From: https://Permalink.Obvsg.At/Ac13082778
5. Razavi A, Stein A, Quirmbach P. Tomographic imaging of bauxite grains leached using hydrochloric acid. Minerals. 2023;13(7):884.
6. Bundesministerium für Wirtschaft und Energie (Bmwi) Öffentlichkeitsarbeit. Für eine starke Stahlindustrie in Deutschland und Europa!: Handlungskonzept Stahl; 2020.
7. Fischedick M, Görner K, Thomeczek M, editors. CO_2: Abtrennung, Speicherung, Nutzung: Ganzheitliche Bewertung im Bereich von Energiewirtschaft und Industrie. Berlin, Heidelberg: Springer Vieweg; 2015.
8. Kircher M, Schwarz T. CO_2 und CO—Nachhaltige Kohlenstoffquellen für die Kreislaufwirtschaft. Berlin, Heidelberg: Springer; 2020.
9. Hegemann K-R, Guder R. Roheisenerzeugung. Wiesbaden: Springer Fachmedien; 2019.
10. Routschka G, Wuthnow H. Praxishandbuch Feuerfeste Werkstoffe: Aufbau—Eigenschaften—Prüfung. 5. Auflage. Essen: Vulkan-Verlag; 2011.
11. Crowley MS. Hydrogen-silica reactions in refractories. Am Ceram Soc Bull. 1967;46(7):679–82.
12. Crowley MS. Hydrogen silica reactions in refractories—part II. Am Ceram Soc Bull. 1970;49(5):527–30.
13. Iso ST, Pask JA. Reaction of silicate glasses and mullite with hydrogen gas. J Am Ceram Soc. 1982;65(8):383–87.
14. Rank J, Melzer D, Wulf B, Anerziris CH, Walter G. Hochtemperaturwärmedämmmaterialien in wasserstoffhaltigen Atmosphären. Cfi/Ber. Dkg. 2008;85(12):17–19.
15. Leber T, Madeo S, Tonnesen T, Telle R. Corrosion of bauxite-based refractory castables and matrix components in hydrogen containing atmosphere. Int J Ceram Eng Sci. 2022;4(1):16–22.
16. Li S, Chen D, Fu L, Zou Y, Huang A, Gu H. Gas corrosion behavior of calcium hexaluminate materials for hydrogen metallurgy. Ceram Int. 2023;49(10):15787–92.
17. Li S, Chen D, Gu H, Huang A, Fu L. Investigation on application prospect of refractories for hydrogen metallurgy: the enlightenment from the reaction between commercial brown corundum and hydrogen. Materials. 2022;15(19):7022.
18. Chemical analysis of refractory products by X-ray fluorescence (XRF) - Fused cast-bead method (ISO 12677:2011). German version EN ISO 12677:2011. 2013.

How to cite this article: Razavi A, Henn I, Sax A, Quirmbach P. X-ray computed tomography study of microstructure weakening by high-temperature hydrogen attack on refractories. Int J Ceramic Eng Sci. 2024;e10211. https://doi.org/10.1002/ces2.10211